

Near-field thermal radiation of germanium selenide single layer

Cheng-Long Zhou,^{1,2} Xiao-Hu Wu,³ Yong Zhang,^{1,2} Hong-Liang Yi ,^{1,2,*} and Dino Novko ^{4,5}¹School of Energy Science and Engineering, Harbin Institute of Technology, Harbin 150001, People's Republic of China²Key Laboratory of Aerospace Thermophysics, Ministry of Industry and Information Technology, Harbin 150001, People's Republic of China³Shandong Institute of Advanced Technology, Jinan 250100, Shandong, People's Republic of China⁴Institute of Physics, Zagreb 10000, Croatia⁵Donostia International Physics Center (DIPC), Donostia-San Sebastián 20018, Spain

(Received 29 July 2021; accepted 30 November 2021; published 16 December 2021)

Recently, the two-dimensional (2D) material germanium selenide (GeSe) was shown to possess extraordinary physicochemical properties as well as great potential for electrical and optical applications, whereas its thermal radiative properties remain elusive. Here, we present a comprehensive study of the near-field thermal radiation (NFTR) of monolayer GeSe by means of fluctuational electrodynamics theory. It is shown that, at a small vacuum gap, such a 2D semiconductor not only supports a giant heat flux that surpasses the black-body limit by four orders of magnitude but is also far ahead of graphene with the same electron density. This extraordinary thermal radiation is attributed to the strong quasi-elliptic surface plasmon polaritons supported by the monolayer GeSe at near- and midinfrared frequency regions. In addition, we show how electron density affects the NFTR of monolayer GeSe, where the effect can be switched from suppression to enhancement by elevating the vacuum gap. Furthermore, we investigate the possibility of using mechanical rotation to modulate the NFTR. We find that, at a lower electron density, the NFTR of the monolayer GeSe could be more effectively modulated through mechanical rotation. Finally, we investigate the interference effect of the dielectric substrate on the NFTR, pointing out the nonmonotonic dependency between its thermal radiation and the dielectric constant of substrate. All in all, in this paper, we provide a fundamental understanding of the NFTR in GeSe single layer and offer guidance for further research and modulation in emerging energy conversion and thermal management.

DOI: [10.1103/PhysRevMaterials.5.124005](https://doi.org/10.1103/PhysRevMaterials.5.124005)

I. INTRODUCTION

In recent years, the exfoliation of graphene from graphite crystals [1] has spurred the drastic development of layered materials, such as borophene [2], hexagonal boron nitride (*h*BN) [3], and germanium selenide (GeSe) [4]. Particularly, as a representative two-dimensional (2D) semiconductor, GeSe has drawn widespread attention due to its unique physical and chemical properties, such as fascinating in-plane anisotropic physical properties, strong light-matter interaction, and enormous piezoelectric effects [5–7]. Unlike black phosphorous, which has the same hinge structure, this 2D semiconductor is less toxic (outstanding environmental compatibility) and has excellent chemical stability in air [8], which makes GeSe more feasible for practical applications in energy storage, sensors, field effect transistors, energy conversion, and so on [9–14]. Specifically, its bandgap of ~ 1.14 eV (optimal photovoltaic bandgap) can greatly improve the efficiency of single-junction solar cells, providing a potential opportunity for photovoltaic applications [15,16]. This 2D anisotropic semiconductor, which has drawn enormous attention recently, shows great potential for a growing range of applications, calling for fundamental study of its thermal properties [17,18]. However, the thermal photon tunneling properties

[i.e., near-field thermal radiation (NFTR)] of this 2D semiconductor are still less known.

Despite the monolayer thickness, contemporary research has unearthed theoretically and experimentally that, by bringing the vacuum gap between two 2D materials into the near field, the thermal photon tunneling phenomenon makes its radiative heat flux (RHF) significantly enhanced and possibly far ahead of the blackbody limit by several orders of magnitude due to its super-strong surface polaritons [19–21]. Ilic *et al.* [22] predicted the super-Planckian thermal radiation properties of graphene sheets in the near field, which spurred the drastic development of the NFTR for many graphene-based configurations, such as graphene grating [23,24], graphene disk [25,26], and graphene/metamaterial heterostructures [27–29]. Other than graphene, with the development of chemosynthesis technology, plenty of 2D materials have been demonstrated to possess extraordinary thermal radiation properties, such as MoS₂ [30], *h* BN [31], and black phosphorus [32,33], bringing tremendous opportunities for thermal management [34–38]. For instance, Shen *et al.* [33] reported that the RHF of monolayer black phosphorus is three orders of magnitude higher than a blackbody at a gap distance of 50 nm. In addition, such huge energy fluxes enabled by 2D materials can also be stimulating for development of numerous futuristic energy conversion technologies [39–42] and radiative information processing [43–45]. For instance, Lim *et al.* [39] reported they covered a InSb thermophotovoltaic

*Corresponding author: yihongliang@hit.edu.cn

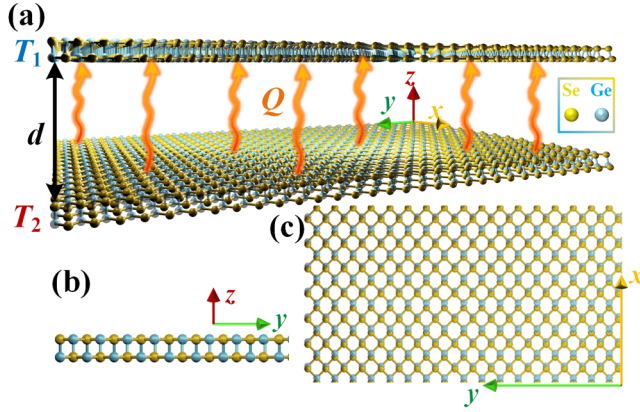


FIG. 1. (a) Near-field thermal radiation between two GeSe sheets with nanoscale vacuum gap d . The bottom and top GeSe sheets have temperature T_2 and T_1 . Schematic of the crystalline structure of GeSe from (b) lateral view and (c) top view. The yellow and blue balls stand for the selenium (Se) atom and germanium (Ge) atom.

cell with a graphene sheet and found that a monolayer of graphene can significantly enhance the power throughput by a factor of 30. Zheng *et al.* [43] proposed that the performance of a thermal diode can be significantly enhanced by the presence of graphene, depending on the hybridization of graphene surface resonance modes with the terminal of the thermal diode. Thus, the systematic prediction and analyzing of the underlying NFTR properties are key to addressing the noncontact thermal management of GeSe-based applications in nanoelectronics, optoelectronics, and thermophotovoltaics and open potential possibility for GeSe-based thermal devices.

To address this knowledge gap, in this paper, we first investigate the extraordinary NFTR of GeSe. By analyzing the photon tunneling coefficient and polariton dispersion, the attribution of the quasi-elliptic surface plasmon polaritons (SPPs), supported by GeSe, to the enhancement of thermal radiation in the near field is examined. After that, we study the effects of the electron density of GeSe and the mechanical rotation as well as the substrate on the NFTR, hoping to provide the guidance to apply GeSe-based materials for active thermal management at the nanoscale. We finally summarize our results at the end.

II. MODEL AND METHODOLOGY

Figure 1(a) exhibits the model of the NFTR between two suspended GeSe sheets with a vacuum gap of d , in which the temperatures of the bottom and top GeSe sheets are fixed as T_2 (310 K) and T_1 (300 K), respectively. The vacuum gap can be flexibly manipulated by the nanopositioner in the experiment [46]. It should be emphasized that investigating suspended 2D materials is a conventional method in the NFTR and can clearly reveal the essential mechanism of thermal photon tunneling properties of 2D materials [47]. As sketched in Figs. 1(b) and 1(c), its crystalline structure is hinglelike, introducing strong anisotropic properties. Compared with black phosphorous, the stronger chemical bonding renders it more stable in air and thus promising for industrial fabrication [48]. Here, we define the armchair and zigzag crystalline directions

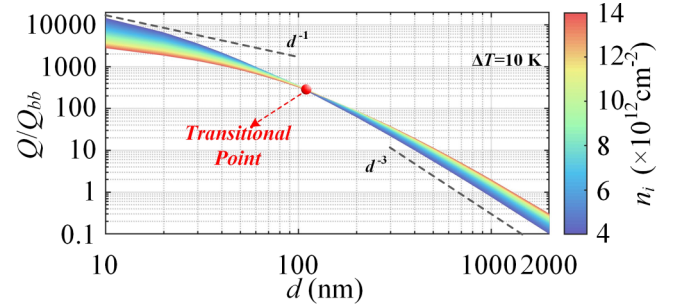


FIG. 2. Normalized radiative heat fluxes (RHF) between the two monolayer GeSe sheets as a function of vacuum gap d at different electron densities. The temperature difference between receiver and emitter is 10 K.

of GeSe sheets as x and y axes, respectively. By solving the fluctuational electrodynamics (FE), the RHF exchanged between the two GeSe sheets can be given by the following Landauer-like expression [49,50]:

$$Q = \int_0^\infty Q(\omega) d\omega = \frac{1}{8\pi^3} \int_0^\infty [\Theta(\omega, T_2) - \Theta(\omega, T_1)] d\omega \times \int_0^\infty \int_0^\infty \xi(\omega, k_x, k_y) dk_x dk_y. \quad (1)$$

Here, $\Theta(\omega, T) = \hbar\omega / [\exp(\hbar\omega/k_B T) - 1]$ stands for the mean energy of the Planck oscillator at the frequency ω and the temperature T . The photonic tunneling coefficient (PTC) $\xi(\omega, k_x, k_y)$ represents the tunneling probability of thermal photons, in which $k_{x,y}$ is the surface wave vector along the x and y axes (related to the calculated method and conductivity tensor of monolayer GeSe, see Supplemental Material [51]).

When the surface parallel wave vector $k = \sqrt{k_x^2 + k_y^2}$ is greater than the wave vector in vacuum, the electromagnetic wave excited by thermal energy is an evanescent wave [52,53]. Otherwise, it is a propagating wave [54].

III. RESULTS AND DISCUSSIONS

We first consider the NFTR between two suspended monolayer GeSe sheets and restrict the vacuum gap in the range of $d \in [10, 2000]$ nm. Regarding the behavior of extreme NFTR < 10 nm, some estimations have been made via experiments and theoretical calculations [55–57]. When the vacuum gap is pushed to ~ 5 nm, the heat transfer of the system would become a complex coupling process among photons, phonons, and electrons [57]. In this paper, to avoid this complicated coupling heat transfer behavior, we chose 10 nm as a minimum vacuum gap. As sketched in Fig. 2, we plotted the normalized RHF Q/Q_{bb} with different electron densities as a function of the vacuum gap d . Here, Q_{bb} is the blackbody limit and can be given by $Q_{bb}(T_1, T_2) = \sigma_{SB}(T_2^4 - T_1^4) \approx 64.36 \text{ W} \cdot \text{m}^{-2}$, in which σ_{SB} is the Stefan-Boltzmann constant. Figure 2 shows that the GeSe sheet can yield distinct near-field enhancement on RHF at a small vacuum gap. Specifically, for a vacuum gap of 10 nm and an electron density of $4 \times 10^{12} \text{ cm}^{-2}$, the RHF can exceed the blackbody limit by four orders of magnitude, even surpassing that of a graphene sheet with the same electron density ($1300 Q_{bb}$) by

11.21 times. However, as the vacuum gap increases, the RHF between the monolayer GeSe sheets exhibits drastic attenuation, and the attenuation tendency gradually transitions from d^{-1} to d^{-3} . When the vacuum gap is restricted to the range of 1000–2000 nm, there is no longer a near-field enhancement effect; that is, this GeSe system yields only an extremely weak RHF (smaller than Q_{bb}), as shown in Fig. 2. The origin of the drastic attenuation can be explained by the two effects: (i) the evanescent wave is easily filtered by a large vacuum gap, resulting in a very weak contribution to the thermal radiation; (ii) due to the optically transparent property, monolayer GeSe cannot effectively absorb propagating waves. As a result, for the vacuum gap of 2000 nm, the RHF between GeSe sheets is significantly smaller than the blackbody limit. Note that the one important aspect of the optical properties of the GeSe sheet is the dependence of the electron density, which can be modulated electrically by introducing external voltage biases [58,59]. In our analysis, the electron density is set in the range of $n_i \in [4, 14] \times 10^{12} \text{ cm}^{-2}$, which is reasonable in the practical synthesis [6].

As shown in Fig. 2, we first notice that, at the deep near field (i.e., the vacuum gap is < 100 nm), the RHF of GeSe is strongly suppressed by the electron density. For example, for $d = 10$ nm, as the electron density increases from 4×10^{12} to $1.4 \times 10^{13} \text{ cm}^{-2}$, the RHF decreases rapidly from $14577 Q_{bb}$ to $2763 Q_{bb}$, and the reduction rate can be as low as 0.19. Moreover, as shown in Fig. 2, the RHF at different vacuum gaps has different responses to the electron density. As the vacuum gap increases to 110 nm, the modulation effect of electron density on RHF is very weak. The maximum percentage of the RHF variation is only 11% (from $265 Q_{bb}$ at $4 \times 10^{12} \text{ cm}^{-2}$ to $294 Q_{bb}$ at $8 \times 10^{12} \text{ cm}^{-2}$). Figure 2 shows that there exists a critical vacuum gap around $d = 110$ nm, where the suppression effect of electron density on thermal radiation would turn into an enhancement effect as the vacuum gap goes beyond the transition point. That is, at the larger gap size, the thermal radiation at higher electron density begins to outperform the ones with low electron density. For $d = 200$ nm, the RHF can increase from $61 Q_{bb}$ at $n_i = 4 \times 10^{12} \text{ cm}^{-2}$ to $89 Q_{bb}$ at $n_i = 1.4 \times 10^{13} \text{ cm}^{-2}$, ~ 1.45 times. As the vacuum gap further increases, the amplification effect of electron density on thermal radiation would be improved rapidly [e.g., $Q(4 \times 10^{12} \text{ cm}^{-2})/Q(1.4 \times 10^{13} \text{ cm}^{-2}) \approx 2.89$ at $\sim 2 \mu\text{m}$].

For more visual observation of the effect of electron density on the NFTR, we exhibit the spectral RHF for a gap $d = 10$ and 200 nm with various electron densities, respectively, in Figs. 3(a) and 3(b). In Fig. 3(a), for $d = 10$ nm, the spectral RHF for $n_i = 4 \times 10^{12} \text{ cm}^{-2}$ can yield a peak as high as $5.24 \text{ nW m}^{-2} \text{ rad}^{-1} \text{ s}$, whereas the maximum of the spectral RHF reduces drastically with increases in n_i . The maxima of spectral RHF decrease to values of 2.63, 1.66, 1.17, and $0.91 \text{ nW m}^{-2} \text{ rad}^{-1} \text{ s}$ for $n_i = 6 \times 10^{12}$, 8×10^{12} , 10^{13} , and $1.2 \times 10^{13} \text{ cm}^{-2}$, respectively, thereby decreasing conspicuously the RHF. Conversely, Fig. 3(a) shows that the influence of the electron density on the spectral bandwidth is negligible for $d = 10$ nm, where the horizontal arrow denotes the bandwidth defined by the full width at half maximum. For the scenario with a larger vacuum gap as sketched in Fig. 3(b), it can be first found that the spectral RHF redshifts to the lower frequencies compared with lower gap under the same electron

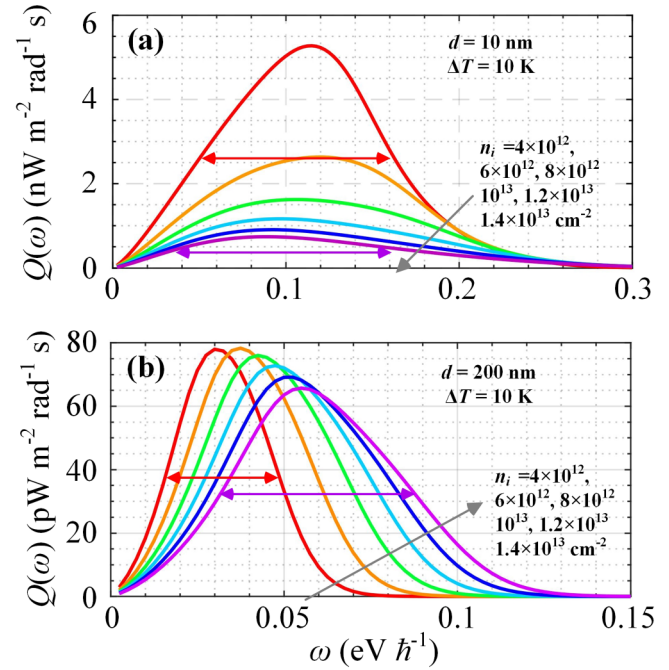


FIG. 3. Spectral radiative heat fluxes (RHF) for a vacuum gap of (a) $d = 10$ nm and (b) $d = 200$ nm. Different line colors indicate different electron densities of GeSe sheet: $n_i = 4 \times 10^{12} \text{ cm}^{-2}$ (red), $n_i = 6 \times 10^{12} \text{ cm}^{-2}$ (orange), $n_i = 8 \times 10^{12} \text{ cm}^{-2}$ (green), $n_i = 10^{13} \text{ cm}^{-2}$ (azure), $n_i = 1.2 \times 10^{13} \text{ cm}^{-2}$ (blue), and $n_i = 1.4 \times 10^{13} \text{ cm}^{-2}$ (purple). The temperature difference between receiver and emitter is 10 K.

density. Moreover, when the vacuum gap increases from 10 to 200 nm, the spectral RHF is reduced significantly. This is the main reason why the thermal radiation with larger vacuum gap is inferior to that of smaller vacuum gap. Physically, it can be explained by the fact that, due to the exponential decay of evanescent waves in vacuum, a larger vacuum gap effectively isolates the coupling between evanescent waves of the emitter and receiver, and therefore, its corresponding contribution to the spectral RHF decreases, as shown in Fig. 3. On the other hand, as shown in Fig. 3, unlike the case at the lower vacuum gap, there is a strong positive correlation between the spectral bandwidth and electron density for $d = 200$ nm. Although the spectral peak decreases with the increasing of n_i , the broader spectral bandwidth can effectively improve the RHF of this system.

To get insight into the physical mechanism of the NFTR of monolayer GeSe, we turn to the PTC and plasmon polariton dispersions. In Figs. 4(a) and 4(b), we calculate the PTC distributions for monolayer GeSe with $d = 10$ nm along the x axis [$\xi(\omega, k_x, 0)$] and y axis [$\xi(\omega, k_y, 0)$], at electron densities of 4×10^{12} , 6×10^{12} , 10^{13} , and $1.4 \times 10^{13} \text{ cm}^{-2}$. The wave vectors along the x and y axes are normalized by the wave vector in vacuum $k_0 = \omega/c$, at which c is the velocity of light in vacuum. As sketched in Figs. 4(a) and 4(b), it can first be found that the bright branches along the x and y directions exhibit great difference. For example, for the electron density of $4 \times 10^{12} \text{ cm}^{-2}$, in Fig. 4(a), the bright branches along the x axis possess a low wave vector region and a broad frequency bandwidth that can extend to $0.35 \text{ eV}/\hbar$. By

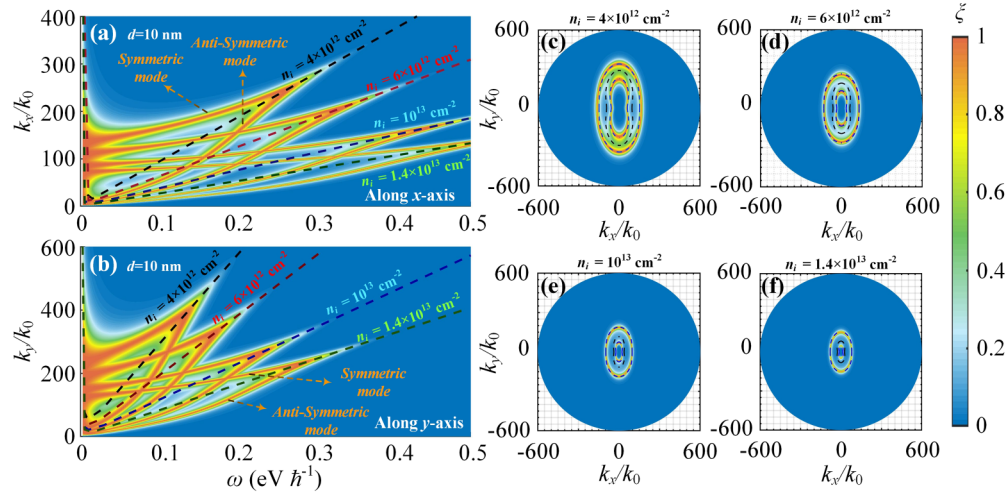


FIG. 4. Photonic tunneling coefficients (PTCs) with different electron densities along (a) the x axis and (b) the y axis. The isofrequency PTC at frequency of $0.1 \text{ eV}/\hbar$ with an electron density of (c) 4×10^{12} , (d) 6×10^{12} , (e) 1×10^{13} , and (f) $1.4 \times 10^{13} \text{ cm}^{-2}$. The vacuum gap is $d = 10 \text{ nm}$. The blue dotted curves represent the polaritons dispersion of antisymmetric and symmetric mode. The dotted curves represent the polaritons dispersion of the monolayer GeSe.

contrast, as shown in Fig. 4(b), although those along the y axis are located in the narrow frequency bandwidth, a higher wave vector region of up to $500 k_0$ can effectively improve the NFTR, especially in the low frequency region. The physical mechanism of this anisotropy along the x and y directions can be revealed by an analysis of the optical conductivity of a monolayer GeSe sheet. We show the imaginary part of the optical conductivity with different electron densities along the x and y axes, respectively, in Figs. 5(a) and 5(b). In all cases, the optical conductivity of the x axis is much larger than that of the y axis, which can be attributed to the difference of the effective mass of electrons between x and y axes. Note that larger effective mass of electrons can excite stronger collective charge oscillations, hence featuring a robust response branch and higher wave vector region, as shown in Fig. 5(b).

Meanwhile, as sketched in Figs. 4(c)–4(f), the isofrequency PTCs $\xi(\omega, k_x, k_y)$ exhibit a quasi-elliptical topological structure, which is consistent with the results predicted by the optical conductivity ($\text{Im}[\sigma_{xx}] > 0$ and $\text{Im}[\sigma_{yy}] > 0$) in Fig. 5. Moreover, as sketched in Figs. 4(a) and 4(b), because of the hybridization mechanism between the SPPs of top and bottom vacuum/GeSe interfaces, two bright branches, i.e., the antisymmetric and symmetric modes, appear. To confirm that

quasi-elliptical SPPs dominate indeed the NFTR between two monolayer GeSe sheets, we exhibit the plasmon polariton dispersion of monolayer GeSe along the x and y directions in Figs. 4(a) and 4(b), respectively. It is shown that all these dotted curves are unambiguously located between the symmetric and antisymmetric modes, which clearly proves that quasi-elliptical SPPs are responsible for the NFTR in this structure. Moreover, with an increase in the electron density, the bright branches along the x and y directions indeed move toward the region of the lower wave vector and become feebler, whereas their bandwidths gradually extend to a broader frequency region, as sketched in Figs. 4(a) and 4(b). To further understand this result, we also show the plasmon polariton dispersions of the GeSe monolayer along the x and y directions at different electron densities. These dispersion curves move toward the region of the lower wave vector monotonically with increasing electron density in Figs. 4(a) and 4(b). Note that this suppression on the wave vector region can be predicted by the optical conductivity. We notice in Fig. 5 that, with the increasing of electron density, the imaginary part of the optical conductivity possesses a higher value, hence increasing the electromagnetic loss and inhibiting the excitation of SPPs at a high wave vector. This also explains unambiguously why the spectral RHF shows a monotonically decreasing trend with an increase in electron density at a vacuum gap of 10 nm , in Fig. 3(a). Meanwhile, for a larger vacuum gap, the large wave vector region of monolayer GeSe with low electron density is easily filtered by vacuum, narrowing the bandwidth of the spectral RHF, as shown in Fig. 3(b).

Note that, as a convenient method of thermal modulation, controlling the relative azimuth between the receiver and emitter (i.e., rotating mechanically the bottom medium) not only effectively controls the NFTR between two anisotropic media but also avoids the introduction of external elements that interfere with the NFTR, such as electrodes and so on [60]. For instance, Liu *et al.* [31] demonstrated a non-contact thermal modulator based on the mechanical rotation between natural van der Waals materials and found that

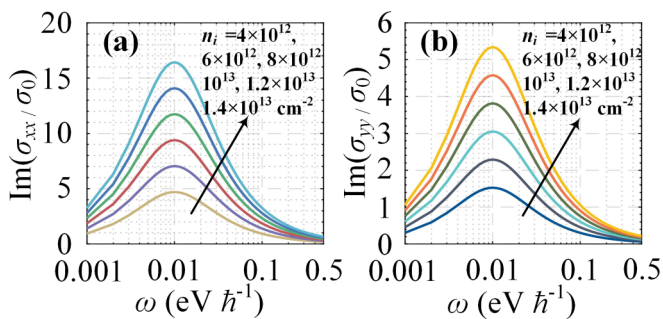


FIG. 5. Imaginary part of the optical conductivity of monolayer GeSe at different electron densities along (a) the x axis and (b) the y axis. The values are normalized by $\sigma_0 = e^2/(4\hbar)$.

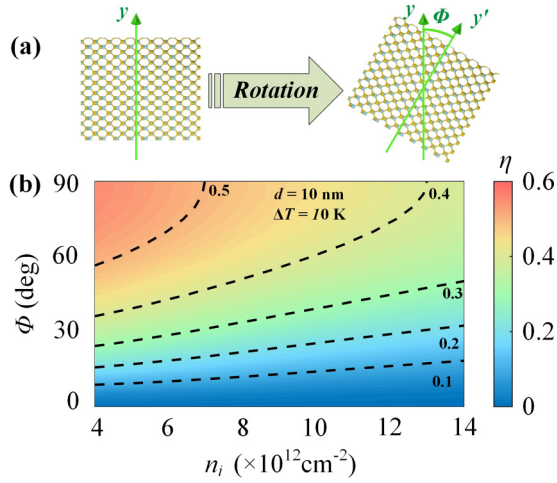


FIG. 6. (a) Top view of the bottom monolayer GeSe sheet at a rotation angle of Φ with respect to the y axis. (b) Tunable factor η corresponding to the twisted monolayer GeSe system with various electron densities. The vacuum gap is fixed as 10 nm.

this thermal modulator can support a high tunable factor [$\eta = 1 - Q(\Phi)/Q(0^\circ)$], reaching > 0.52 at a gap distance of 10 nm. As shown in Fig. 6(a), through rotating the bottom monolayer GeSe sheet by an angle of Φ with respect to the y axis, the symmetry between two monolayer GeSe sheets would be destroyed, thus effectively regulating the NFTR of this system. In what follows, we analyze in detail the performance of using the mechanical rotation to control the NFTR between two monolayer GeSe sheets. Here, we normalize the modulation effect of mechanical rotation on the NFTR as a tunable factor for a fixed electron density.

As shown in Fig. 6(b), the tunable factor increases along with the rotation angle for all electron densities, implying the RHF exhibits monotonic attenuation vs the rotation angle. For larger electron density of $1.4 \times 10^{13} \text{ cm}^{-2}$, while the bottom monolayer GeSe sheet is twisted through the external mechanical torque, the tunable factor can elevate up to 0.39 for $\Phi = 90^\circ$, which implies that the NFTR between two monolayer GeSe sheets can be modulated effectively by the rotation angle. As the electron density enters the lower doping region, Fig. 6(b) shows that compared with the configurations at high electron density, the mechanical rotation can yield more efficient modulation on the thermal radiation of the monolayer GeSe. For instance, when the electron density is doped to $4 \times 10^{12} \text{ cm}^{-2}$, we find that the maximal tunable factor can be raised to 0.56, as sketched in Fig. 6(b). To understand clearly the modulation effect of mechanical rotation on the NFTR, the spectral RHF for an electron density $n_i = 4 \times 10^{12}$ and $1.4 \times 10^{13} \text{ cm}^{-2}$ with different mechanical rotation angles are shown in Fig. 7. It can be found that the spectral RHF decreases rapidly with the increasing rotation angle, and its maximum possesses an obvious decrease from 5.27 to $2.32 \text{ nW m}^{-2} \text{ rad}^{-1} \text{ s}$; that is nearly 0.44 times. This can also contribute to the understanding of the high-efficiency modulation effect of mechanical rotation on RHF at lower electron density. While we further dope GeSe to $1.4 \times 10^{13} \text{ cm}^{-2}$, the decreasing trend of spectral RHF induced by mechanical rotation is significantly weaker, in which the maximum of

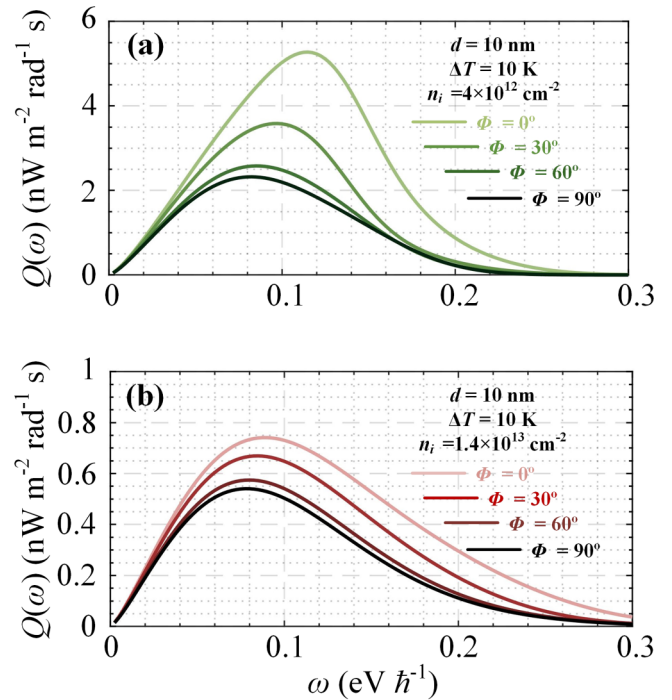


FIG. 7. Spectral radiative heat fluxes (RHF) with electron density of (a) $4 \times 10^{12} \text{ cm}^{-2}$ and (b) $1.4 \times 10^{13} \text{ cm}^{-2}$ for a rotation angle of 0° , 30° , 60° , and 90° . The vacuum gap is fixed as 10 nm.

spectral RHF only reduces from 0.74 to $0.54 \text{ nW m}^{-2} \text{ rad}^{-1} \text{ s}$, as sketched in Fig. 7(b).

To get additional insight into the origin of the modulation effect of mechanical rotation on the NFTR, the PTCs between two monolayer GeSe sheets with rotation angles of 30° , 60° , and 90° are plotted in Fig. 8. The electron densities of Figs. 8(a) and 8(b) are fixed to 4×10^{12} and $1.4 \times 10^{13} \text{ cm}^{-2}$, respectively. The frequency and the vacuum gap are chosen to be $0.1 \text{ eV}/\hbar$ and 10 nm, respectively. Meanwhile, we also show the plasmon polariton dispersion in Fig. 8, in which the black and red dotted lines represent the polariton dispersion of the top and bottom monolayer GeSe sheets for a mechanical rotation angle of Φ , respectively. It is clearly demonstrated that the PTC between two monolayer GeSe sheets can be significantly influenced while the bottom monolayer GeSe sheet is rotated by an angle of Φ . Figure 8(a) shows that, for $n_i = 4 \times 10^{12} \text{ cm}^{-2}$, with the increase in the angle, the high values of PTC can be induced only in the region where the polariton dispersions between two monolayer GeSe sheets overlap. It can be explained that, for the lower electron density, when the polariton dispersion extends to a higher value of wave vector, the monolayer GeSe sheet could yield a more pronounced decoupling effect by manipulating the rotation angle, therefore leading to a noteworthy decrease in RHF, as indicated in Figs. 6 and 7. In addition, for the higher electron density, we notice that, as the bottom sheet is rotated, the PTC between two monolayer GeSe sheets would exhibit a weaker decoupling phenomenon [see Fig. 8(b)]. This weaker decoupling remodels the bright branches of the PTC from elliptical to quasirhombic, in which the optical axis of the polariton dispersions on the top and bottom GeSe sheets always corresponds to the convex corner of the quasirhombic bright

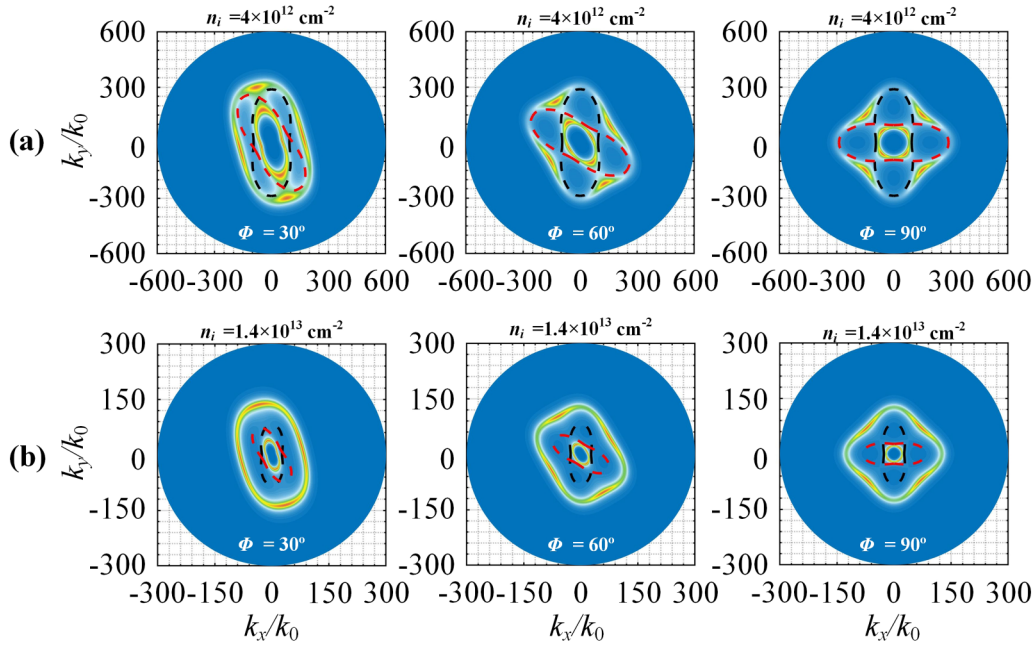


FIG. 8. Photonic tunneling coefficients (PTCs) for $\Phi = 30^\circ, 60^\circ,$ and 90° with electron density of (a) $4 \times 10^{12} \text{ cm}^{-2}$ and (b) $1.4 \times 10^{13} \text{ cm}^{-2}$. The black and red dotted lines correspond to the plasmon polariton dispersions of the top and bottom monolayer GeSe sheets with a rotation angle of Φ , respectively. The vacuum gap is 10 nm. The frequency is $0.1 \text{ eV}/\hbar$.

branches. Notably, at $n_i = 1.4 \times 10^{13} \text{ cm}^{-2}$, Fig. 8(b) shows that, as the rotation angle increases, the region with high values of PTC in the resonance branch gradually decreases, which is the main reason responsible for the decreasing NFTR in Figs. 6 and 7; however, the weaker decoupling cannot substantively curtail the coupling range between the surface states of the two monolayer GeSe sheets in k space, thereby resulting in a smaller modulation effect on the NFTR.

Although suspended 2D material sheets can be realized technically in experiments, it is difficult to use this suspension technology in applications in thermal control [61]. Here, 2D material sheets are generally deposited on a substrate [62–64]. Therefore, as shown in Fig. 9, exploring the NFTR of a monolayer GeSe sheet on different substrates has a strong guiding significance for experiments and various application development. The interference effect of a substrate on the NFTR of a monolayer GeSe sheet is demonstrated in Fig. 9(a). To avoid the uncertainty caused by complex polariton hybrid effect, in this section, the dielectric substrate is chosen as a nonpolar and nondispersive material. In Fig. 9(a), the RHF with various electron densities possess a similar trend with respect to the dielectric constant ϵ_s of the substrate. For example, at $n_i = 4 \times 10^{12} \text{ cm}^{-2}$, it can be observed that the RHF first exhibits an increasing tendency (from $7726 Q_{bb}$ at $\epsilon_s = 0.1$ to $17332 Q_{bb}$ at $\epsilon_s = 2$) and then decreases to $4126 Q_{bb}$ at $\epsilon_s = 10$, as shown in Fig. 9(a). In other words, to ensure outstanding RHF, the thermal device based on a monolayer GeSe sheet should avoid a substrate with too large a dielectric constant. To provide some visual insight into the interference effect of the substrate on the NFTR, we present in Fig. 9(c) the spectral RHF of a monolayer GeSe sheet with various dielectric substrates. Here, the electron density is chosen as $4 \times 10^{12} \text{ cm}^{-2}$. As the dielectric constant of the substrate increases from 0.1 to 10, we can observe that the spectral peak

shows a nonmonotonic dependency vs the dielectric constant. When the dielectric constant of the substrate is replaced from 0.1 to 2, as shown in Fig. 9(c), the spectral peak increases

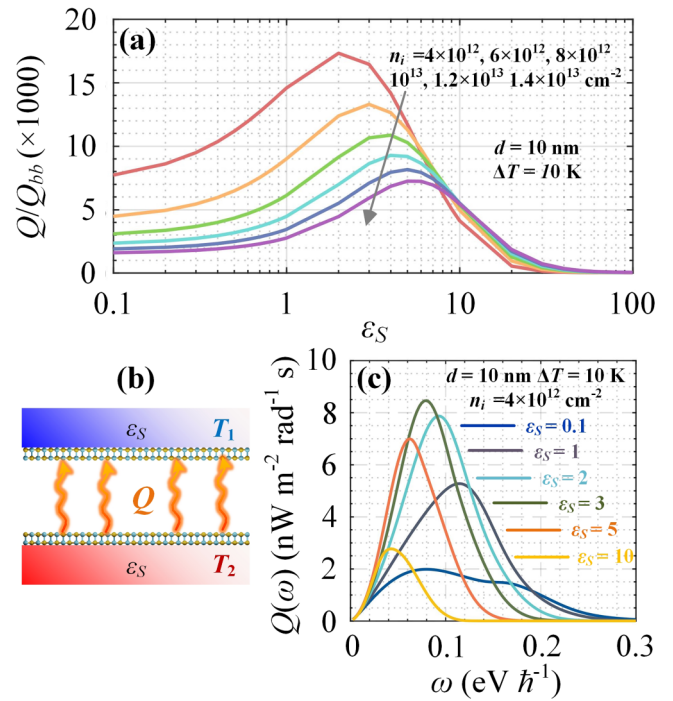


FIG. 9. (a) Radiative heat fluxes (RHF) for the coating system as a function of the dielectric constant ϵ_s of substrate for different electron densities. (b) Schematic of near-field thermal radiation (NFTR) of the coating system. (c) Spectral RHF as a function of frequency for different dielectric substrates with electron density of $4 \times 10^{12} \text{ cm}^{-2}$. The vacuum gap is $d = 10 \text{ nm}$.

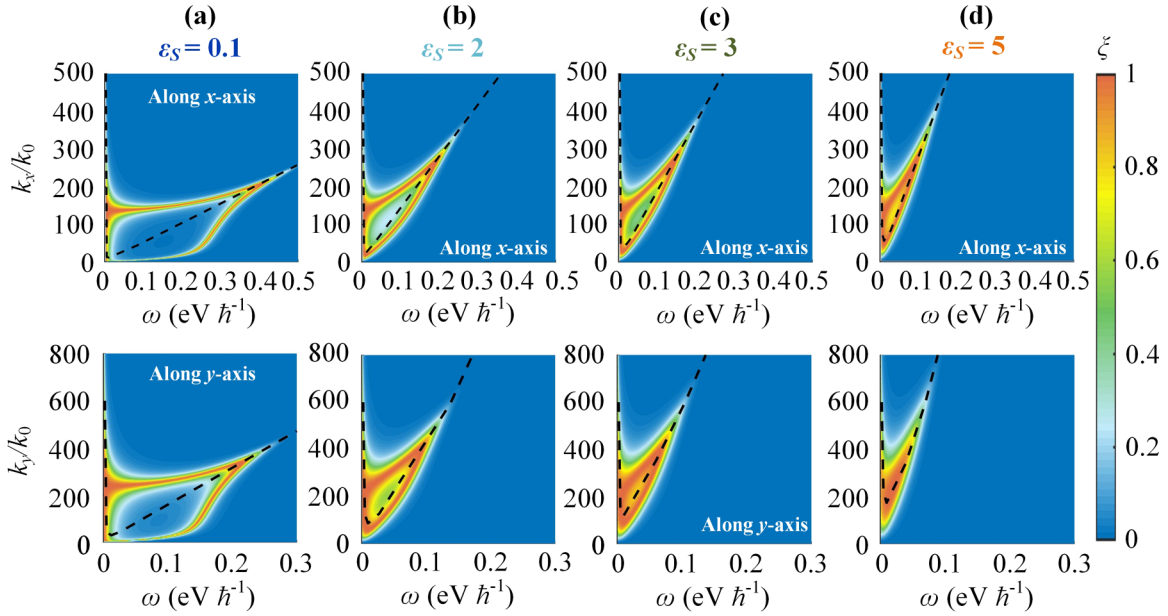


FIG. 10. Photonic tunneling coefficients (PTCs) along the x axis (top column) and the y axis (bottom column) for different dielectric substrates: (a) $\epsilon_s = 0.1$, (b) $\epsilon_s = 2$, (c) $\epsilon_s = 3$, and (d) $\epsilon_s = 5$. The black dash line corresponds to the polariton dispersion of the coating system. The vacuum gap is $d = 10$ nm. The electron density is 4×10^{12} cm $^{-2}$.

from 1.98 to 7.86 nW m $^{-2}$ rad $^{-1}$ s, which corresponds to the sharp increasing in the NFTR in Fig. 9(a); however, as the dielectric constant increases to 3, although the RHF peaks at 8.46 nW m $^{-2}$ rad $^{-1}$ s, the narrow spectral response deteriorates the NFTR between two monolayer GeSe sheets, in which the spectral bandwidth defined by the full width at half maximum decreases from 0.086 eV/ \hbar at $\epsilon_s = 2$ to 0.076 eV/ \hbar at $\epsilon_s = 3$. With further increase in the dielectric constant of the substrate, Fig. 9(c) shows the spectral RHF reduces gradually and is compressed to a narrower frequency region. As a result, for a dielectric constant of 10, this coating system yields only the RHF of 4126 Q_{bb} .

To provide some physical insight into the interference effect of a substrate on the NFTR, we present in Fig. 10 the PTCs along the x axis [top column] and y axis [bottom column] for different dielectric substrates chosen from a set of $\epsilon_s = 0.1, 2, 3$, and 5. The vacuum gap is $d = 10$ nm. The electron density is 4×10^{12} cm $^{-2}$. Under all scenarios, the plots along the x and y axes exhibit great differences, in which the bright branches along the x axis occupy in the region with broad spectral bandwidth and low wave vector. Moreover, it should be noted that, as the dielectric constant of the substrate increases from 0.1 to 3, the bright branches along the x and y axes move toward a larger wave vector, resulting in increasing spectral peaks. However, continuing to increase the dielectric constant would lead to a thinner resonance branch of PTC, thereby considerably reducing the spectral response of a monolayer GeSe sheet in Fig. 9(b). Meanwhile, as the dielectric constant of the substrate increases, the bright band branches corresponding to the symmetric and antisymmetric modes gradually come close to each other. When the dielectric constant of the substrate is 5, the symmetrical and antisymmetric branches of SPPs form a continuous region with a near-unity value in the $\omega - k_{x,y}$ phase space, as shown in Fig. 10. This is because a substrate with a larger dielectric

constant would effectively interfere with the hybridization between the SPPs of top and bottom vacuum/GeSe interfaces. Meanwhile, with the increasing of the substrate dielectric constant, the resonance branch of PTC and the dispersion relations along the x and y axes gradually move toward the low frequency region, as shown in Fig. 10.

IV. CONCLUSIONS

In conclusion, we study the NFTR between two monolayer GeSe sheets and discover that monolayer GeSe can yield a giant NFTR that is four orders of magnitude greater than for a blackbody, even exceeding graphene sheets with the same electron density by 11.21 times. Through observation on the photon tunneling coefficient and dispersion relations, we demonstrate the dominant role of quasi-elliptic SPPs on thermal photon tunneling at near- and midinfrared frequency regions. We further propose that the NFTR of monolayer GeSe could be controlled effectively through the electron density and mechanical rotation. It is found that high electron density in monolayer GeSe greatly restrains the exciting of the quasi-elliptic SPPs modes with a high wave vector, allowing the heat flux to be decreased effectively. Moreover, with the decreasing of electron density, the decoupling effect induced by mechanical rotation can be enhanced, achieving more effective active control of the NFTR. Finally, the interference effect of the substrate on the NFTR of monolayer GeSe is explored. It is shown that the coating structure exhibits a nonmonotonic dependency of its thermal radiation on the dielectric constant of the substrate. The underlying mechanism is mainly attributed to the higher wave vector of the SPPs with a bigger dielectric constant of the substrate. Our results not only firstly give insight into the NFTR between the GeSe sheets, i.e., a natural 2D semiconductor with intrinsic in-plane anisotropy, but also pave the way to apply GeSe-based

materials for active thermal management in nanoelectronics, optoelectronics, and thermoelectricity.

ACKNOWLEDGMENTS

This paper was supported by the National Natural Science Foundation of China (Grant No. 52076056), the Fundamen-

tal Research Funds for the Central Universities (Grant No. FRFCU5710094020), the Shandong Provincial Natural Science Foundation (Grant No. ZR2020LLZ004), the Croatian Science Foundation (Grant No. UIP-2019-04-6869), and the European Regional Development Fund for the “Center of Excellence for Advanced Materials and Sensing Devices” (Grant No. KK.01.1.1.01.0001).

-
- [1] A. K. Geim and K. S. Novoselov, The rise of graphene, *Nat. Mater.* **6**, 183 (2007).
- [2] A. J. Mannix, X. F. Zhou, B. Kiraly, J. D. Wood, D. Alducin, B. D. Myers, X. L. Liu, B. L. Fisher, U. Santiago, and J. R. Guest, Synthesis of borophenes: Anisotropic, two-dimensional boron polymorphs, *Science* **350**, 1513 (2015).
- [3] Y. Kubota, K. Watanabe, O. Tsuda, and T. Taniguchi, Deep ultraviolet light-emitting hexagonal boron nitride synthesized at atmospheric pressure, *Science* **317**, 932 (2007).
- [4] D.-J. Xue, J. Tan, J.-S. Hu, W. Hu, Y.-G. Guo, and L.-J. Wan, Anisotropic photoresponse properties of single micrometer-sized GeSe nanosheet, *Adv. Mater.* **24**, 4528 (2012).
- [5] G. S. Shi and E. Kioupakis, Anisotropic spin transport and strong visible-light absorbance in few-layer SnSe and GeSe, *Nano Lett.* **15**, 6926 (2015).
- [6] W. He, H. Chen, H. Ouyang, J. Zhou, Y. Sui, C. Zhang, X. Zheng, R. Zhang, X. Yuan, Z. Xu, and X. Cheng, Tunable anisotropic plasmon response of monolayer GeSe nanoribbon arrays, *Nanoscale* **12**, 16762 (2020).
- [7] M. H. Wu and X. C. Zeng, Intrinsic ferroelasticity and/or multiferoicity in two-dimensional phosphorene and phosphorene analogues, *Nano Lett.* **16**, 3236 (2016).
- [8] S. C. Liu, Y. Mi, D. J. Xue, Y. X. Chen, C. He, X. Liu, J. S. Hu, and L. J. Wan, Investigation of physical and electronic properties of GeSe for photovoltaic applications, *Adv. Electron. Mater.* **3**, 1700141 (2017).
- [9] Y. J. Ji, M. Y. Yang, H. L. Dong, T. J. Hou, L. Wang, and Y. Y. Li, Two-dimensional germanium monochalcogenide photocatalyst for water splitting under ultraviolet, visible to near-infrared light, *Nanoscale* **9**, 8608 (2017).
- [10] M. Y. Wang, L. H. Li, G. H. Zhao, Z. W. Xu, S. Hussain, M. S. Wang, G. J. Qiao, and G. W. Liu, Influence of the surface decoration of phosphorene with Ag nanoclusters on gas sensing properties, *Appl. Surf. Sci.* **504**, 144374 (2020).
- [11] C. Luo, X. D. Guo, H. Hu, D. B. Hu, C. C. Wu, X. X. Yang, and Q. Dai, Probing polaritons in 2D materials, *Adv. Opt. Mater.* **8**, 1901416 (2020).
- [12] Z. Y. Yang, L. Liao, F. Gong, F. Wang, Z. Wang, X. Q. Liu, X. H. Xiao, W. D. Hu, J. He, and X. F. Duan, WSe₂/GeSe heterojunction photodiode with giant gate tenability, *Nano Energy* **49**, 103 (2018).
- [13] H. Li, P. P. Xu, and J. Lu, Sub-10 nm tunneling field-effect transistors based on monolayer group IV mono-chalcogenides, *Nanoscale* **11**, 23392 (2019).
- [14] J. W. Villanova and S. Barraza-Lopez, Anomalous thermoelectricity at the two-dimensional structural transition of SnSe monolayers, *Phys. Rev. B* **103**, 035421 (2021).
- [15] X. T. Wang, Y. Y. Li, L. Huang, X. W. Jiang, L. Jiang, H. L. Dong, Z. M. Wei, J. B. Li, and W. P. Hu, Short-wave near-infrared linear dichroism of two-dimensional germanium selenide, *J. Am. Chem. Soc.* **139**, 14976 (2017).
- [16] Y. L. Mao, C. S. Xu, J. M. Yuan, and H. Q. Zhao, A two-dimensional GeSe/SnSe heterostructure for high performance thin-film solar cells, *J. Am. Chem. Soc.* **7**, 11265 (2019).
- [17] G. Z. Qin, Z. Z. Qin, W. Z. Fang, L. C. Zhang, S. Y. Yue, Q. B. Yan, M. Hu, and G. Su, Diverse anisotropy of phonon transport in two-dimensional group IV–VI compounds: a comparative study, *Nanoscale* **8**, 11306 (2016).
- [18] P. F. Liu, T. Bo, J. P. Xu, W. Yin, J. R. Zhang, F. W. Wang, O. Eriksson, and B. T. Wang, First-principles calculations of the ultralow thermal conductivity in two-dimensional group-IV selenides, *Phys. Rev. B* **98**, 235426 (2018).
- [19] S. A. Biehs, R. Messina, P. S. Venkataram, A. W. Rodriguez, J. C. Cuevas, and P. Ben-Abdallah, Near-field radiative heat transfer in many-body systems, *Rev. Mod. Phys.* **93**, 025009 (2021).
- [20] J. C. Cuevas and F. J. Garcia-Vidal, Radiative heat transfer, *ACS Photon.* **5**, 3896 (2018).
- [21] Z. M. Zhang, *Nano/Microscale Heat Transfer* (Springer, Cham, 2020).
- [22] O. Ilic, M. Jablan, J. D. Joannopoulos, I. Celanovic, H. Buljan, and M. Soljačić, Near-field thermal radiation transfer controlled by plasmons in graphene, *Phys. Rev. B* **85**, 155422 (2012).
- [23] X. L. Liu and Z. M. Zhang, Giant enhancement of nanoscale thermal radiation based on hyperbolic graphene plasmons, *Appl. Phys. Lett.* **107**, 143114 (2015).
- [24] M. J. He, H. Qi, Y. T. Ren, Y. J. Zhao, and M. Antezza, Magneto-plasmonic manipulation of nanoscale thermal radiation using twisted graphene gratings, *Int. J. Heat. Mass. Tran.* **150**, 119305 (2020).
- [25] F. V. Ramirez and A. J. H. McGaughey, Plasmonic thermal transport in graphene nanodisk waveguides, *Phys. Rev. B* **96**, 165428 (2017).
- [26] F. V. Ramirez, S. Shen, and A. J. H. McGaughey, Near-field radiative heat transfer in graphene plasmonic nanodisk dimers, *Phys. Rev. B* **96**, 165427 (2017).
- [27] K. Z. Shi, Y. C. Sun, Z. Y. Chen, N. He, F. L. Bao, J. Evans, and S. L. He, Colossal enhancement of near-field thermal radiation across hundreds of nanometers between millimeter-scale plates through surface plasmon and phonon polaritons coupling, *Nano Lett.* **19**, 8082 (2019).
- [28] J. Yang, W. Du, Y. S. Su, Y. Fu, S. X. Gong, S. L. He, and Y. G. Ma, Observing of the super-Planckian near-field thermal radiation between graphene sheets, *Nat. Commun.* **9**, 4033 (2018).
- [29] B. Zhao, B. Guizal, Z. M. Zhang, S. H. Fan, and M. Antezza, Near-field heat transfer between graphene/h BN multilayers, *Phys. Rev. B* **95**, 245437 (2017).

- [30] J. B. Peng, G. Zhang, and B. W. Li, Measuring the thermal conductivity and interfacial thermal resistance of suspended MoS_2 using electron beam self-heating technique, *Appl. Phys. Lett.* **107**, 133108 (2015).
- [31] X. L. Liu, J. D. Shen, and Y. M. Xuan, Pattern-free thermal modulator via thermal radiation between Van der Waals materials, *J. Quant. Spectrosc. Ra.* **200**, 100 (2017).
- [32] Y. Zhang, H. L. Yi, and H. P. Tan, Near-field radiative heat transfer between black phosphorus sheets via anisotropic surface plasmon polaritons, *ACS Photon.* **5**, 3739 (2018).
- [33] J. D. Shen, S. Guo, X. L. Liu, B. Liu, W. T. Wu, and H. He, Super-Planckian thermal radiation enabled by coupled quasi-elliptic 2D black phosphorus plasmons, *Appl. Therm. Eng.* **144**, 403 (2018).
- [34] K. Z. Shi, F. L. Bao, and S. L. He, Near-field heat transfer between graphene-Si grating heterostructures with multiple magnetic-polaritons coupling, *ACS Photon.* **4**, 971 (2017).
- [35] N. H. Thomas, M. C. Sherrott, J. Broulliet, H. A. Atwater, and A. J. Minnich, Electronic modulation of near-field radiative transfer in graphene field effect heterostructures, *Nano Lett.* **19**, 3898 (2019).
- [36] O. Ilic, N. H. Thomas, T. Christensen, M. C. Sherrott, M. Soljačić, A. J. Minnich, O. D. Miller, and H. A. Atwater, Active radiative thermal switching with graphene plasmon resonators, *ACS Nano* **12**, 2474 (2018).
- [37] X. L. Liu, J. D. Shen, and Y. M. Xuan, Near-field thermal radiation of nanopatterned black phosphorene mediated by topological transitions of phosphorene plasmons, *Nanosc. Microsc. Therm.* **23**, 188 (2019).
- [38] P. Ben-Abdallah, A. Belarouci, L. Frechette, and S. A. Biehs, Heat flux splitter for near-field thermal radiation, *Appl. Phys. Lett.* **107**, 053109 (2015).
- [39] M. Lim, S. Jin, S. S. Lee, and B. J. Lee, Graphene-assisted Si-InSb thermophotovoltaic system for low temperature applications, *Opt. Express* **23**, A240 (2015).
- [40] V. B. Svetovoy and G. Palasantzas, Graphene-on-Silicon Near-Field Thermophotovoltaic Cell, *Phys. Rev. Applied* **2**, 034006 (2014).
- [41] R. St-Gelais, G. R. Bhatt, L. X. Zhu, S. H. Fan, and M. Lipson, Hot carrier-based near-field thermophotovoltaic energy conversion, *ACS Nano* **11**, 3001 (2017).
- [42] R. Messina and P. Ben-Abdallah, Graphene-based photovoltaic cells for near-field thermal energy conversion, *Sci. Rep.* **3**, 1383 (2013).
- [43] Z. H. Zheng, X. L. Liu, A. Wang, and Y. M. Xuan, Graphene-assisted near-field radiative thermal rectifier based on phase transition of vanadium dioxide (VO_2), *Int. J. Heat. Mass. Transfer* **109**, 63 (2017).
- [44] H. M. Wang, J. H. Li, J. H. Edgar, and X. G. Xu, Three-dimensional near-field analysis through peak force scattering-type near-field optical microscopy, *Nanoscale* **12**, 1817 (2020).
- [45] H. Hu, X. X. Yang, F. Zhai, D. B. Hu, R. N. Liu, K. H. Liu, Z. P. Sun, and Q. Dai, Far-field nanoscale infrared spectroscopy of vibrational fingerprints of molecules with graphene plasmons, *Nat. Commun.* **7**, 12334 (2016).
- [46] M. Ghashami, H. Geng, T. Kim, N. Iacopino, S. K. Cho, and K. Park, Precision Measurement of Phonon-Polaritonic Near-Field Energy Transfer between Macroscale Planar Structures Under Large Thermal Gradients, *Phys. Rev. Lett.* **120**, 175901 (2018).
- [47] O. D. Miller, O. Ilic, T. Christensen, M. T. H. Reid, H. A. Atwater, J. D. Joannopoulos, M. Soljacic, and S. G. Johnson, Limits to the optical response of graphene and two-dimensional materials, *Nano Lett.* **17**, 5408 (2017).
- [48] S. P. Poudel and S. Barraza-Lopez, Metastable piezoelectric group-IV monochalcogenide monolayers with a buckled honeycomb structure, *Phys. Rev. B* **103**, 024107 (2021).
- [49] S. A. Biehs, F. S. S. Rosa, and P. Ben-Abdallah, Modulation of near-field heat transfer between two gratings, *Appl. Phys. Lett.* **98**, 243102 (2011).
- [50] E. Moncada-Villa, V. Fernandez-Hurtado, F. J. Garcia-Vidal, A. Garcia-Martin, and J. C. Cuevas, Magnetic field control of near-field radiative heat transfer and the realization of highly tunable hyperbolic thermal emitters, *Phys. Rev. B* **92**, 125418 (2015).
- [51] See Supplemental Material at <http://link.aps.org/supplemental/10.1103/PhysRevMaterials.5.124005> for (1) the Drude model for the conductivity of monolayer GeSe, (2) expression for PTCs of the anisotropic monolayer GeSe, and (3) plasmon dispersion formulation for GeSe, which includes Refs. [65–75].
- [52] W. B. Zhang, C. Y. Zhao, and B. X. Wang, Enhancing near-field heat transfer between composite structures through strongly coupled surface modes, *Phys. Rev. B* **100**, 075425 (2019).
- [53] J. Y. Chang, P. Sabbaghi, and L. P. Wang, Near-field radiative heat transfer between nanowire-based dual uniaxial magneto-dielectric metamaterials, *Int. J. Heat. Mass. Transfer.* **158**, 120023 (2020).
- [54] J. DeSutter, L. Tang, and M. Francoeur, A near-field radiative heat transfer device, *Nat. Nanotechnol.* **14**, 751 (2019).
- [55] B. Song, D. Thompson, A. Fiorino, Y. Ganje, P. Reddy, and E. Meyhofer, Radiative heat conductances between dielectric and metallic parallel plates with nanoscale gaps, *Nat. Nanotechnol.* **11**, 509 (2016).
- [56] L. J. Cui, W. Jeong, V. Fernandez-Hurtado, J. Feist, F. J. Garcia-Vidal, J. C. Cuevas, E. Meyhofer, and P. Reddy, Study of radiative heat transfer in Ångström-and nanometre-sized gaps, *Nat. Commun.* **8**, 14479 (2017).
- [57] T. Tokunaga, A. Jarzembki, T. Shiga, K. Park, and M. Francoeur, Extreme near-field heat transfer between gold surfaces, *Phys. Rev. B* **104**, 125404 (2021).
- [58] T. Low, R. Roldán, H. Wang, F. Xia, P. Avouris, L. Moreno, and F. Guinea, Plasmons and Screening in Monolayer and Multilayer Black Phosphorus, *Phys. Rev. Lett.* **113**, 106802 (2014).
- [59] L. Xu, M. Yang, S. J. Wang, and Y. P. Feng, Electronic and optical properties of the monolayer group-IV monochalcogenides MX ($M = \text{Ge}, \text{Sn}; X = \text{S}, \text{Se}, \text{Te}$), *Phys. Rev. B* **95**, 235434 (2017).
- [60] G. M. Tang, J. Chen, and L. Zhang, Twist-induced control of near-field heat radiation between magnetic Weyl semimetals, *ACS Photon.* **8**, 443 (2021).
- [61] J. C. Meyer, A. K. Geim, M. I. Katsnelson, K. S. Novoselov, T. J. Booth, and S. Roth, The structure of suspended graphene sheets, *Nature (London)* **446**, 60 (2007).
- [62] X. D. Guo, H. Hu, X. Zhu, X. X. Yang, and Q. Dai, Higher order Fano graphene metamaterials for nanoscale optical sensing, *Nanoscale* **9**, 14998 (2017).
- [63] B. Zhang, J. L. Song, L. Lu, B. W. Li, K. Zhou, Q. Cheng, and Z. X. Luo, Magnetic-field control of near-field radiative heat transfer between graphene-based hyperbolic metamaterials, *Appl. Phys. Lett.* **117**, 163901 (2020).

- [64] N. Youngblood and M. Li, Integration of 2D materials on a silicon photonics platform for optoelectronics applications, *Nanophotonics* **6**, 1205 (2017).
- [65] A. Nemilentsau, T. Low, and G. Hanson, Anisotropic 2D Materials for Tunable Hyperbolic Plasmonics, *Phys. Rev. Lett.* **116**, 066804 (2016).
- [66] C. L. Zhou, X. H. Wu, Y. Zhang, and H. L. Yi, Super-Planckian thermal radiation in borophene sheets, *Int. J. Heat. Mass. Tran.* **183**, 122140 (2022).
- [67] A. Lakhatakia, Green's functions and Brewster condition for a half space bounded by an anisotropic impedance plane, *Int. J. Infrared Milli.* **13**, 631 (1992).
- [68] J. S. Gomez-Diaz, M. Tymchenko, and A. Alù, Hyperbolic metasurfaces: surface plasmons, light-matter interactions, and physical implementation using graphene strips, *Opt. Mater. Express* **5**, 2313 (2015).
- [69] H. J. Bilow, Guided waves on a planar tensor impedance surface, *IEEE Trans. Antenn. Propag.* **51**, 2788 (2003).
- [70] M. Q. Yuan, Y. Zhang, S. H. Yang, and H. L. Yi, Active control of the near-field radiative heat transfer between two metal plates through the external electric field, *Int. J. Therm. Sci.* **171**, 107208 (2022).
- [71] M. Nakayama, Theory of surface waves coupled to surface carriers, *J. Phys. Soc. Jpn.* **36**, 393 (1974).
- [72] K. W. Chiu and J. J. Quinn, Plasma oscillations of a two-dimensional electron gas in a strong magnetic field, *Phys. Rev. B* **9**, 4724 (1974).
- [73] O. V. Kotov and Y. E. Lozovik, Hyperbolic hybrid waves and optical topological transitions in few-layer anisotropic metasurfaces, *Phys. Rev. B* **100**, 165424 (2019).
- [74] T. Zhan, X. Shi, Y. Y. Dai, X. H. Liu, and J. Zi, Transfer matrix method for optics in graphene layers, *J. Phys.: Condens. Matter* **25**, 215301 (2013).
- [75] P. Yeh, Electromagnetic propagation in birefringent layered media, *J. Opt. Soc. Am.* **69**, 742 (1979).